2
Microfluidic Networks*

Norbert Kockmann

2.1
Introduction

Microfluidic networks are essential elements for numbering-up and scale-up of high-throughput, microstructured devices, microscale heat exchangers and heat spreaders. A uniform flow distribution over stacked elements is necessary for high-performance devices. A flow maldistribution would dramatically lower the device's performance and diminish miniaturization effects [1].

Beginning with fundamentals of fluid dynamics, correlations for the pressure loss in channel elements are presented, which are concatenated to fluidic networks to distribute fluid homogeneously over a certain area. Computational fluid dynamic (CFD) simulations of single elements are exploited for analytical pressure loss correlations. These are employed in lumped element modeling of networks and manifolds, which are too complex for direct simulations. Design strategies and methods are presented for channel networks, manifolds for parallel channels on a plate and headers for stacked-plate devices.

2.2
Fluid Mechanics

The flow in microchannels is often dominated by viscous forces leading to straight laminar flow. Here, single-phase flow is treated without any influence of surface or interface forces. The flow regime in channels is characterized by the Reynolds number, *Re*, which is the ratio of the momentum force and viscous force:

$$Re = \frac{\text{momentum force}}{\text{viscous force}} = \frac{w d_h}{\nu} \tag{2.1}$$

with mean flow velocity w, kinematic viscosity ν and hydraulic diameter $d_h = 4A/l_P$. The hydraulic diameter is the characteristic length of the flow situation, for example,

*List of Symbols can be found at the end of this chapter.

Micro Process Engineering, Vol.1: Fundamentals, Operations and Catalysts
Edited by V. Hessel, A. Renken, J.C. Schouten, and J.-I. Yoshida

ISBN: 978-3-527-31550-5

the diameter in circular pipe flow or twice the gap height in slit flow. For low Reynolds numbers, $Re < 10$, viscous forces dominate the flow and diminish vortex generation. With higher Reynolds numbers, vortices appear in curved flow and, above a critical value Re_{crit}, vortices appear in straight channels and the flow becomes unsteady and turbulent. In channel flow, this transition to turbulent flow happens at Reynolds numbers of ~2300 [2].

The balance equations for mass, momentum and energy describe the entire flow situation. The continuity assumption of smooth fluid properties and no-slip flow conditions at the wall hold for most cases in microprocess engineering, hence the change in density ρ with time is correlated with the velocity vector w as

$$\frac{D\rho}{Dt} + \rho \mathrm{div}\,\vec{w} = 0 \tag{2.2}$$

The momentum equation is expressed by the Navier–Stokes equation in vector form:

$$\rho \frac{D\vec{w}}{Dt} = \rho\left(\frac{\partial}{\partial t} + \vec{w}\,\mathrm{div}\right)\vec{w}$$

$$= \rho\,\vec{g}\text{-}\mathrm{grad}\,p + \mathrm{Div}\left[\eta\left(2\mathrm{grad}\,\vec{\mathbf{w}} - \frac{2}{3}\vec{\delta}\;\mathrm{div}\,\vec{w}\right)\right]$$

$$\text{with} \qquad \mathrm{grad}\;\vec{\mathbf{w}} = \frac{1}{2}\left[\mathrm{grad}\;\vec{w} + (\mathrm{grad}\;\vec{w})^{\mathrm{T}}\right] \tag{2.3}$$

The energy equation can be derived from the first law of thermodynamics or the equilibrium of kinetic and potential energy:

$$p_2 + \frac{\rho}{2}w_2^2 - \rho g y_2 = p_1 + \frac{\rho}{2}w_1^2 - \rho g y_1 + w_{t12} - \varphi_{12} \tag{2.4}$$

This equation is also called the Bernoulli equation, where the energy dissipation φ_{12} is equal to the pressure loss Δ_p in the channel. In microchannels without mechanical devices ($w_t = 0$), the potential energy of height variation dy can often be neglected. With these assumptions, the pressure loss in a channel element with variable cross section can be calculated from

$$\Delta p = p_1 + \frac{\rho}{2}w_1^2 - p_2 - \frac{\rho}{2}w_2^2 = \sum_i \left(\lambda_i \frac{l_i}{d_{h,i}} + \zeta_i\right)\frac{\rho}{2}w_{ref}^2 \tag{2.5}$$

The terms in the sum consist of the channel friction factor λ_i and the pressure loss coefficient of channel internals or fittings ζ_i. For laminar flow in straight channels, the channel friction factor λ_i is inversely proportional to the Reynolds number in the channel:

$$\lambda_i = \frac{C_f}{Re} = \frac{C_f \nu}{w d_h} \tag{2.6}$$

The friction coefficient C_f depends on the cross-section of the channel and equals 64 for circular tubes, 56.92 for square channels and 96 for fluid flow in a narrow gap

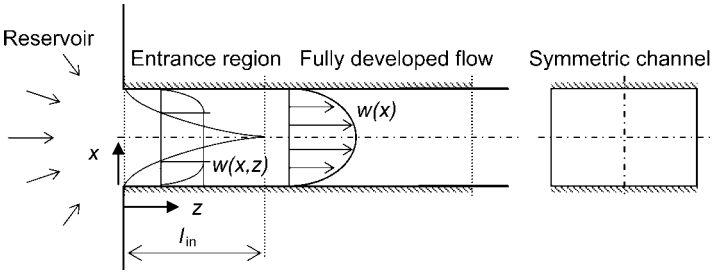

Figure 2.1 Entrance flow with developing flow profile in a channel.

(slit flow). Other values can be found in [3]. For turbulent flow, the channel friction factor is independent of the flow velocity (and *Re*) and depends only on the surface roughness of the channel. The transition regime between straight laminar flow and turbulent flow can be approximated by square fitting of the laminar and turbulent friction factor:

$$\lambda_{\text{transition}} = \sqrt{\lambda_{\text{laminar}}^2 + \lambda_{\text{turbulent}}^2} \tag{2.7}$$

Aside from straight laminar microchannels, the flow in entrance, bends, curves and fittings is important for full characterization of fluidic networks. At the entrance of a channel, the flow starts to develop its profile due to the wall friction. In laminar flow, the entrance length is defined where 99% of the parabolic flow profile is achieved in the channel. The flow situation is displayed in Figure 2.1 for fully developed and entrance flow in a channel element.

In laminar flow for $Re < 2000$, the entrance length l_{in} depends on the Reynolds number [2, 4]:

$$\frac{l_{\text{in}}}{d_{\text{h}}} = 0.056\, Re \tag{2.8}$$

or, with a more complex correlation

$$\frac{L_{\text{in}}}{d_{\text{h}}} = \frac{C_1}{1 + C_2\, Re/C_1} + C_2\, Re \tag{2.9}$$

	C_1	C_2
circular pipe:	1.2	0.224
rectangular channel:	0.89	0.164

The coefficients C_1 and C_2 depend on the geometry of the channel cross-section. The pressure loss in the entrance region is given by Knoeck [5] as

$$\Delta p = \frac{32}{\sqrt{6 d_{\text{h}}}} \eta w \tag{2.10}$$

for pipes with circular cross-section and

$$\Delta p = \frac{24}{\sqrt{3 d_{\text{h}}}} \eta w \tag{2.11}$$

for a narrow gap, where η is the dynamic viscosity.

The flow and pressure loss in entrance, bends and curves for $Re < 10$ can be described with the help of straight laminar flow correlations. With higher Reynolds numbers, centrifugal forces generate vortices, which cause additional pressure loss, as described in the next section.

2.3 Basic Channel Structures

To set up a complete channel network, bends and T-joints are the main elements, which are described in the following concerning flow regimes and pressure loss.

Flow in bends is characterized by the Reynolds number, bend angle and radius. The radius is introduced in the dimensionless Dean number, Dn, which is closely related to Re:

$$Dn = Re\sqrt{\frac{d_h}{2R}} \tag{2.12}$$

The Dean number originates from curved tube flow; for rectangular cross-sections and sharp bends, the hydraulic diameter and the mean flow radius substitute the original lengths [6]. The flow is straight laminar in bends for $Dn < 10$. For higher Dean numbers, a counter-rotating double vortex is generated in the bend. For $Dn > 140$, a secondary double vortex appears at the outer wall of the bend (see Figure 2.3). In Figure 2.2, three different bends are displayed with pressure loss dependent on the Reynolds number. The dotted line indicates the laminar flow pressure loss in a straight channel with same length. The pressure loss in the straight channel for transitional flow with approximately $100 < Re < Re_{crit}$ can be expressed as a power function of the Reynolds number:

$$\Delta p = p_1 - p_2 = \frac{C_f}{Re^{0.35}} \frac{l}{d_h} \frac{\rho}{2} w_{ref} \tag{2.13}$$

resulting in the correlation of the pressure loss with the velocity, $\Delta p \propto w_{ref}^{1.65}$. The cross-section before and after the bend is uniform, hence the velocity does not change after the bend, $w_1 = w_2$. Using Equation (2.5), the pressure loss over the bend is calculated as

$$\Delta p = \zeta_b \frac{\rho}{2} w_1^2 \tag{2.14}$$

with bend pressure loss coefficient ζ_b. In the range $50 < Re < 400$, the coefficient ζ_b is 2.56 ± 0.15 for the sharp 90° bend and 1.68 ± 0.16 for the radius bend. The values originate from CFD simulations (CFD-ACE+ from ESI group) of the liquid flow (water, 20 °C) in microchannels with square cross-section of $300 \times 300\,\mu m$.

In Figure 2.3, the flow regimes and pressure loss in T-joints are displayed for divergent flow. The side view clearly indicates the double vortex in the curved flow. In 90° bends, a secondary vortex pair is formed at higher Reynolds numbers ($Re > 500$). The T-joint with a wedge has a triangular-like wall shape at the stagnation point,

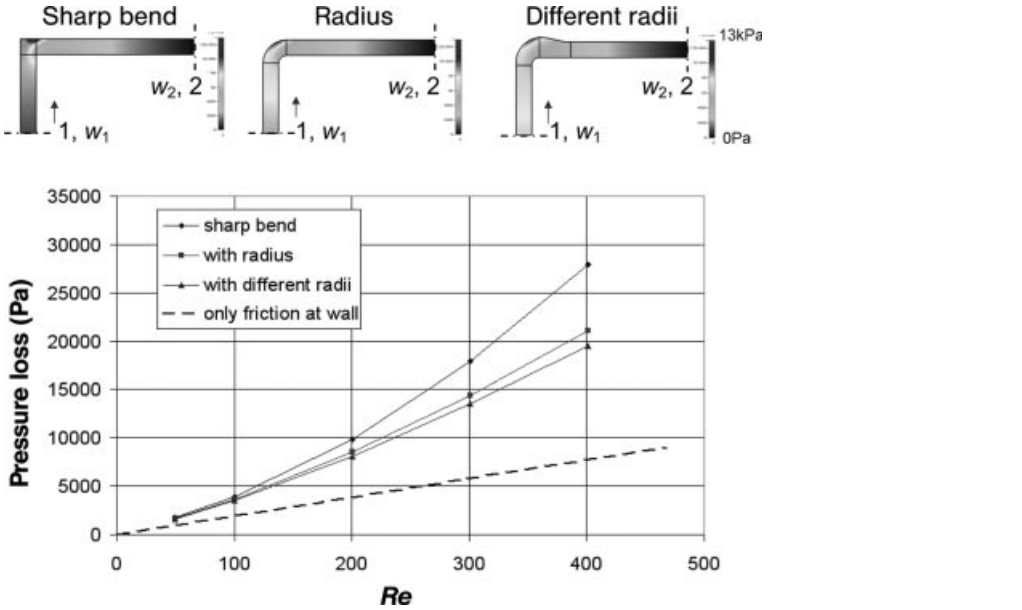

Figure 2.2 Three different bends with pressure distribution along the middle axis. The pressure loss over the Reynolds number in the channel deviates from straight laminar flow (straight dotted line). The steady CFD simulations did not converge for $Re > 400$.

which notably decreases the pressure loss. The Reynolds number changes behind the joint, hence a pressure loss coefficient ζ_b is formed for the inlet velocity. For a 90° T-joint, the coefficient ζ_b is ~1.9 and increases with increase in *Re*, whereas the coefficient ζ_b for the wedge T-joint is 1.35 and decreases with increase in *Re*. The

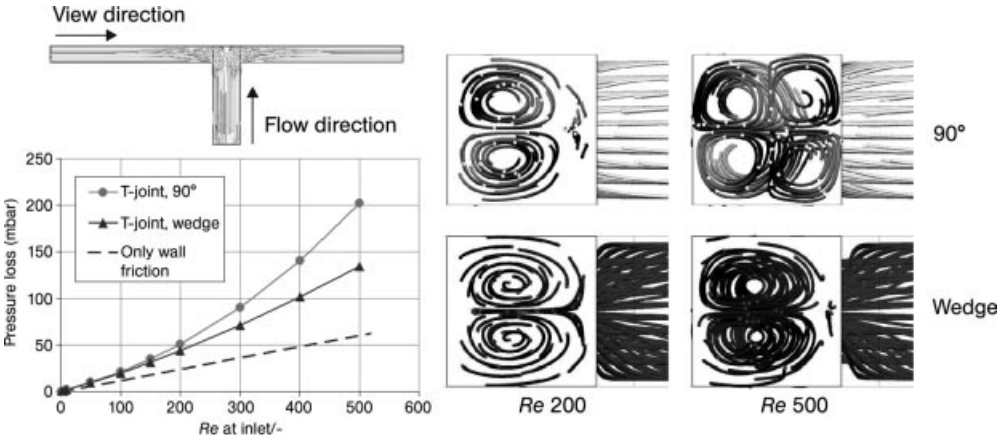

Figure 2.3 Flow regimes and pressure loss in a T-joint with divergent flow. The steady CFD simulations did not converge for $Re > 500$.

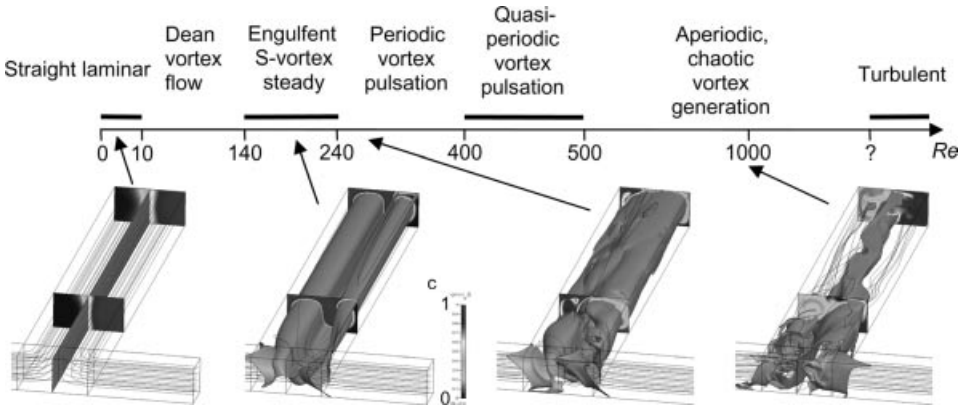

Figure 2.4 Flow regimes in a T-joint with convergent flow and symmetrical inlet flow conditions [7, 8].

wedge reduces the pressure loss due to a smoothed flow situation and fewer vortices in bend flow.

The flow situation changes when the T-joint is used for converging flow, often used as mixing element. Figure 2.4 displays the flow regimes in a T-joint with converging flow for Reynolds numbers ranging from creeping flow ($Re = 0.01$) to chaotic flow for $Re > 400$.

More information on laminar flow in channels and ducts can be found in publications by Knoeck [5] and Shah and London [9]. Transient flow regimes in T-shaped micromixers have a large influence on mixing and chemical reactions [10].

2.4 Network Design

Channel networks are used to spread fluid over an area for cooling purposes, to supply channel elements for mixing or for other purposes. Two design methods are used here: the constructal theory of Bejan [11] for network arrangement and the biomimetic correlation of cross-sectional areas on different branching levels, the so-called Murray's law. This law was applied by Emerson *et al.* [12] and Chen and Cheng [13] for the design of fluidic networks in electronic cooling.

The constructal design approach begins with the smallest elements on the zero level and connects these with those on the next higher level. This approach works inversely to the fractal description of branched systems where an element is repeatedly miniaturized until almost infinitely small structures. In nature, systems have a finite smallest size and, hence, follow the constructal approach. The optimum size of channel elements and the corresponding area covered depend on the transport velocity of the important quantity, such as the heat flux [14, 15]. Here, the constructal method is applied to area coverage; Bello-Ochende *et al.* [16] presented a three-dimensional constructal network for cooling purposes.

The size of channel cross-sections on different branching levels can be determined by another biological principle given by Murray's law, which describes the branching of blood vessels [17] or plant capillaries [18]. This law was observed in biological systems, such as plants [19] and mammals [20]. The application of this biomimetic rule leads to a channel network with low wall shear stress in the channels, which might be one reason for the biological occurrence [17]. In these biological systems, the sum of the inner radii to the power of 3 is constant on each branching level. With this condition, the wall shear stress is constant for all branching levels and the pressure loss depends mainly on the channel length. For channels with circular cross-section, the diameter of the highest and largest level element d_n to the power of 3 is equal to the sum of the diameters d_z of the next level elements to the power of 3. In channels with non-circular cross-section, the radius is replaced by the hydraulic diameter:

$$d_{\mathrm{h},0}^3 = \sum_i d_{\mathrm{h},i}^3 \tag{2.15}$$

In channel networks, often bifurcations occur where the flow splits into two equal mass flows. For this case, Murray's law can be given as

$$d_{\mathrm{h},1} = d_{\mathrm{h},0} \times 2^{-1/3} \tag{2.16}$$

for one bifurcation and for z levels

$$d_{\mathrm{h},z} = d_{\mathrm{h},0} \times 2^{-z/3} \tag{2.17}$$

Murray's law applied to cooling systems results in structures similar to Figure 2.5 and leads to branched systems and devices as displayed in Figure 2.6. The pressure loss in a network can be calculated with lumped element modeling and with the help of electronic circuit layout routines; see the next section and Sack *et al.* [21].

A fabricated silicon chip (40×40 mm footprint) with unidirectional, fork-like structures is displayed in Figure 2.6. The width and height of the entrance

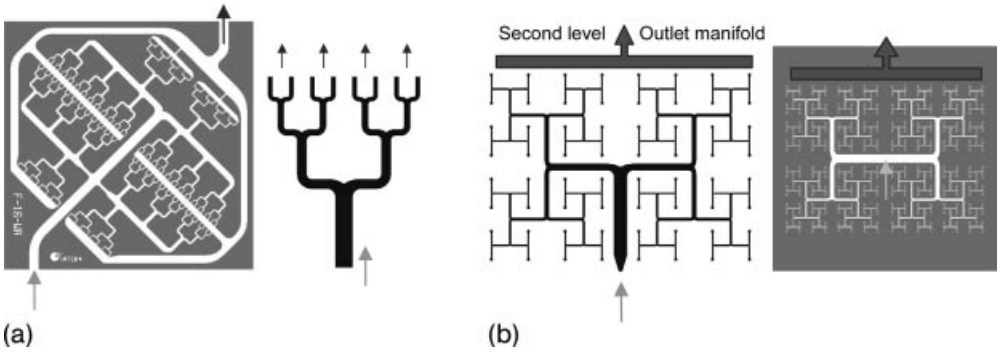

Figure 2.5 Principle setup of two-dimensional, constructal network: (a) Unidirectional network with fork-like structure and four levels; (b) bidirectional network with antenna-like structure and six levels.

Figure 2.6 Fabricated silicon chip with dendritic channel system for cooling purposes; 40 × 40 mm footprint.

microchannel were 1500 and 300 µm, respectively. The uniform flow distribution was validated by optical observation of a colored flow pulse. The pressure loss over the entire device was 430 mbar at a water flow rate of 4.2 kg h^{-1}. An overall heat transfer coefficient of 3.5 kW m^{-2} K^{-1} was measured at this flow rate. It was confirmed experimentally that the thermal efficiency (defined as heat transfer rate per unit power required) of such fork-like microchannel heat sink is much higher than that of a conventional heat sink with parallel microchannels for the same heat transfer rate, temperature difference and inlet velocity.

2.5 Lumped Element Modeling

CFD simulations in Section 2.3 gave pressure loss coefficients for single channel elements. Combined microfluidic networks, such as given in the previous section, can only be treated by numerical methods with enormous effort. Hence the pressure loss in the flow manifold in Figure 2.6 is determined by lumped element modeling with tolerable effort, here according the flow resistance method [22]. The electric resistance is defined as electric potential divided by the electric flow (the voltage divided by the current). The fluidic flow is the mass flow rate, while the potential can be expressed with two different possibilities. The simpler one is to use the pressure as potential, where the fluidic resistance is given by

$$R_{\mathrm{fl}} = \frac{\Delta p}{\dot{m}} \tag{2.18}$$

A more complex way is to define the potential in such a way that the product of potential and flow delivers the power. This leads to the introduction of the mechanical potential. For smaller velocities the mechanical potential is equal to the constant energy in the Bernoulli equation, Eq. (2.4). The resulting resistance is a nonlinear

cross-section resistance. The advantage of this resistance is the ability to calculate the single resistances for either viscous losses or losses due to the redirection of the flow or the changing of the cross-section. Unfortunately, this advantage only holds for fully developed flows, for example, in a bent channel the flow has to be fully developed in front of the bend and must have enough space to redevelop the laminar flow profile after the bend. The flow in the investigated networks is not developed, hence the latter method is not used.

In order to homogenize the pressure loss from the inlet to each single branch and from each single branch to the outlet, the shorter channels are narrowed at some point (see Figure 2.6). The aim is to adjust at least the pressure resistance due to wall friction from the inlet to each single branch and from every branch to the outlet. The fluid that flows through the branch at the bottom end of the chip has a much longer route to the outlet than the fluid that flows through the branch at the top end of the chip. Hence the fluid that leaves the upper branch is forced to flow through a very narrow channel. The width of this narrow channel is calculated using Equation (2.18) and the correlations given in Equations (2.6), (2.13) and (2.14), giving a rough approximation for the pressure resistance. The pressure resistance of one branch is higher than that of the supply channel or the manifold channel; however, the mass flow rate is much lower in the single branches. For the developed design, the pressure loss due to wall friction in the branches is only about 10% of the overall pressure loss due to wall friction in the whole device. The equivalent pressure resistance of one branch is about 2–3 times higher than the resistance of the supply and manifold channels, but the flow rate is up to 16 times smaller. The pressure-optimized design for the branches will have only a small influence on the overall pressure loss.

As an additional example, micromixers with high flow rates are presented where the parallel mixing elements are connected with inlet and outlet manifolds [23]. In Figure 2.7, a micromixer (20×20 mm footprint) with 16 parallel mixing elements is shown together with meandering mixing channels and outlet manifold.

The aim of the manifold design is the uniform fluid distribution on each mixing element with a mixing ratio of 1:1 for a chemical reaction. The pressure drop from the

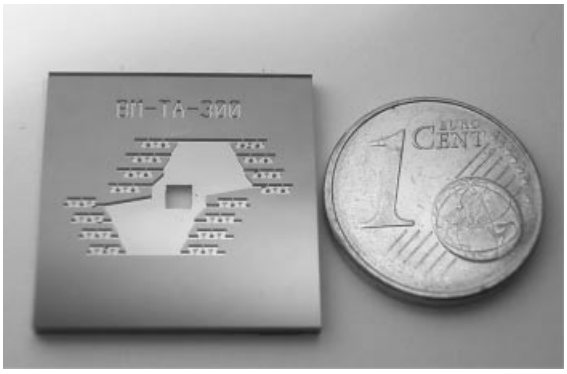

Figure 2.7 Silicon micromixer chip for high mass flow rates; 20×20 mm footprint.

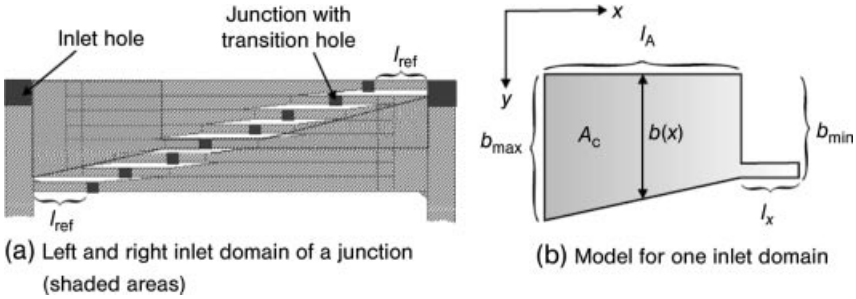

Figure 2.8 Schematic setup of the inlet distribution for eight parallel mixing elements, here the upper half of the 3D-T mixer without assisting precursor bends.

inlet over the single mixing element to the outlet hole determines the flow rate through each element. The model to determine the pressure loss for the inlet manifold is sketched in Figure 2.8. A wide channel distributor and a small single channel, whose length is adjusted to yield a uniform pressure loss for all mixing elements, give the model of the inlet manifold. A reference length of one inlet channel is defined on which the pressure drop of the other inlet channels is adjusted. The common large area A_C represents the widening of the other channels and the following single remaining inlet channels; see the marked area in Figure 2.8a.

To simplify the calculations, the flow in the manifold is regarded as straight laminar, because analytical or numerical determination of the real flow behavior in this domain is too complex. Since entrance effects and other nonlinear phenomena occur on both sides of the joint, the pressure loss in these elements is disregarded. If the inlet channel includes a bend, the channel system is symmetrically arranged to guarantee the same pressure drop behavior for a wide flow rate range, as shown in Figure 2.9.

The pressure drop across this model structure (Figure 2.8b) is now balanced with the pressure drop Δp_{ref} through the reference channel. Using Equation (2.4), the pressure drop per unit length can be calculated with the channel friction factor, the hydraulic diameter and the mean velocity:

$$\frac{\Delta p}{\Delta l} = \frac{\lambda_i}{d_h}\frac{\rho}{2}\bar{w}^2 \tag{2.19}$$

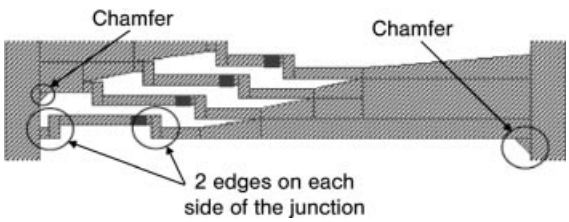

Figure 2.9 Schematic setup of the inlet distribution for eight parallel mixing elements, here 3D-T mixer with assisting precursor bends.

With laminar flow and constant C_f, the pressure drop across the area A_C [constant height h and variable width $b(x)$] is approximated by

$$\Delta p_{A_C} \approx \int_0^{l_A} \frac{C_f \dot{m} \eta [b(x)+h]^2}{\rho [b(x)h]^3} \mathrm{d}x \tag{2.20}$$

substituting the mean velocity by the mass flow rate $\dot{m}$. The friction coefficient C_f is dependent on the geometry and can be determined for rectangular cross-section according to Sharp *et al.* [3]. With the pressure drop Δp_{ch} through the remaining channel and the total length $l_{tot} = l_x + l_A$ of the inlet domain, the correlation to calculate the length l_x of the remaining channel is given by

$$\Delta p_{ref} = \Delta p_{ch} + \Delta p_{A_C}$$

$$\Delta p_{ref} = \frac{C_f \dot{m} \eta}{\rho} \left[\frac{l_x (b_{ch}+h)^2}{(b_{ch}h)^3} + \int_0^{l_{tot}-l_x} \frac{[b(x)+h]^2}{[b(x)h]^3} \mathrm{d}x \right], \tag{2.21}$$

with the width of the remaining channel b_{ch}. The pressure drop Δp_{ref} through the reference channel is determined by applying the channel length l_{ref} to Equation (2.20):

$$\Delta p_{ref} = \frac{C_f \dot{m} \eta l_{ref} (b_{ch}+h)}{\rho (b_{ch}h)^3} \tag{2.22}$$

The combination of Equations (2.21) and (2.22) gives the length of each inlet channel for the single mixing elements. The factor $C_f \dot{m} \eta / \rho$ cancels out on both sides and the above equations were iteratively solved for l_x. The entrance length of each mixing element is dependent on the reference channel length and the manifold geometry.

The entire pressure loss in the outlet manifold results from the last section of the mixing channel and the collecting zone of the outlet (Figure 2.10b). Due to the relatively low pressure loss and the wide outlet section, a rough estimation of the length of the mixing channel gives an appropriate uniform pressure loss for all mixing elements. First, the end section of the mixing channel closest to the outlet hole is set to a length of 1000 µm (Figure 2.10b).

The fluid path from the mixing channel outlet to the chip outlet is measured for the most probable length of a fluid element, which is not necessarily a straight line. With this graphical method, the length of the fluid path of each mixing element is determined. The pressure drop in the outlet manifold is linearly dependent on this length and is determined with a reference pressure drop:

$$\Delta p_{ref} = \Delta p_{ch} + \Delta p_{man} \tag{2.23}$$

For simplicity, the pressure drop over the single channel elements is proportional to the friction factor and the ratio of the length to the width:

$$\Delta p_{ch} \propto C_f \frac{l_{ch}}{b_{ch}} \tag{2.24}$$

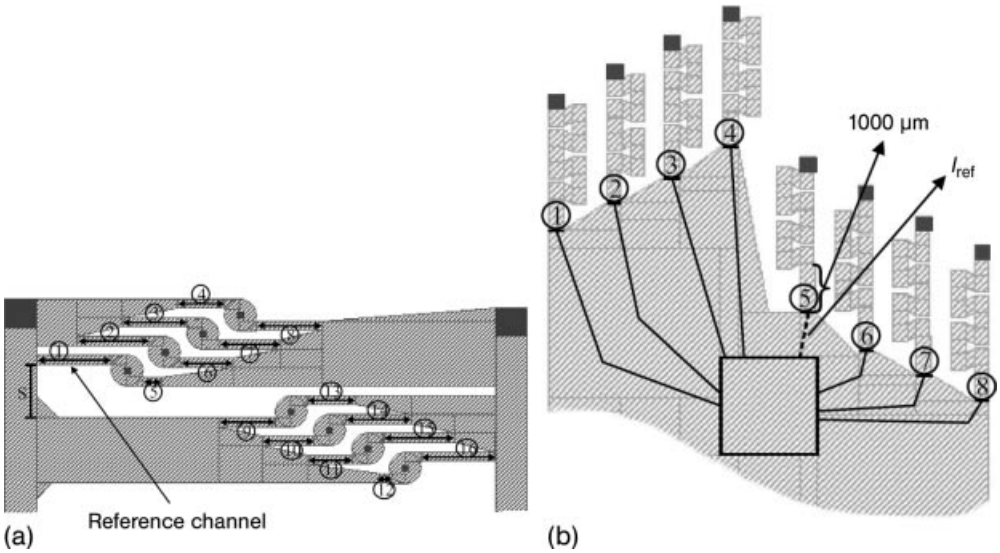

Figure 2.10 Determining the length of the entire mixing device with inlet and outlet distribution.

With the reference pressure loss in the mixing channel closest to the outlet hole, which has to be determined for the actual case, the channel length of the single mixing elements can be determined with the following equation:

$$l_{ch} \propto b_{ch}\left(\Delta p_{ref} - \frac{l_{man}}{b_{man}}\right) \tag{2.25}$$

The uniform flow distribution was optically determined using mixing and a color pH indicator, and also with the selectivity of a parallel-competitive reaction, which was the same for mixing in single mixer elements and in devices with 16 parallel elements.

2.6 Parallel Channel Devices

In microfluidic devices, often several straight channels are arranged in parallel on one plate to increase the mass flow rate. Adequate flow manifolds must be provided to supply each channel uniformly for utilizing the benefits of miniaturization. In Figure 2.11, CFD simulation results of conventional inlet and outlet manifold design are given together with the normalized flow rate distribution over parallel channels [24]. The original type B-1 induces a flow maldistribution of ~5%. Enlargement of the inlet zone (type B-3) has no larger influence on the maldistribution, whereas enlargement of the outlet zone (type B-2) reduces the maldistribution below 1%. The

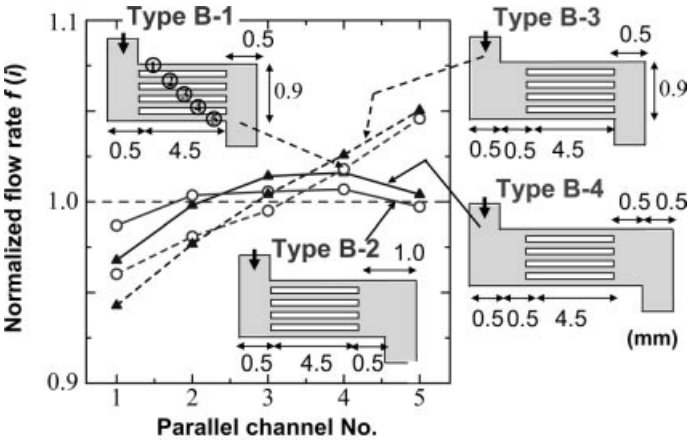

Figure 2.11 Effect of inlet and outlet shape on flow distribution in parallel channels, according to Tonomura [24].

enlargement of both inlet and outlet zones (type B-4) produces a greater maldistribution than type B-2. It is interesting that the outlet design has the largest influence on the flow distribution, although the outlet causes a very low pressure loss. The impact of the pressure loss at the entrance is larger due to the low absolute pressure at the outlet of the device. For example, if the pressure losses at the entrance and the outlet are 200 and 100 mbar, respectively, and the entire pressure loss over the device is 4 bar starting from an entrance pressure of 5 bar, the relative pressure loss at the entrance is 4% in comparison with 10% at the exit. This simple example clearly illustrates the importance of the outlet pressure loss, but the situation of a real device must be considered in more detail.

The entire pressure loss in this device is calculated from mass flow rate and the contributing channel parts of inlet, channel and outlet:

$$\begin{aligned}\Delta p &= \Delta p_{\text{in}} + \Delta p_{\text{ch}} + \Delta p_{\text{out}} \\ &= (\zeta_{\text{in}} + \lambda_{\text{ch}} + \zeta_{\text{out}})\frac{\rho}{2} w_{\text{ch}}^2\end{aligned} \tag{2.26}$$

Pfeifer *et al.* [25] measured the exit velocity distribution behind a plate with parallel channels and compared their results with numerical simulations. The flow velocity was measured with a hot wire anemometer (5 µm diameter, 2 mm long). They found that the gaps between foils have a strong influence on the flow distribution.

In addition to rectangular inlet and outlet flow distributions, wedge-shaped geometries have a positive effect on the uniform distribution, as displayed in Figure 2.12.

Figure 2.12 indicates the important role of the inlet/outlet manifold on the uniform flow distribution to each channel. The wedge-shaped design realizes a uniform flow distribution and avoids deterioration of the reactor performance [26].

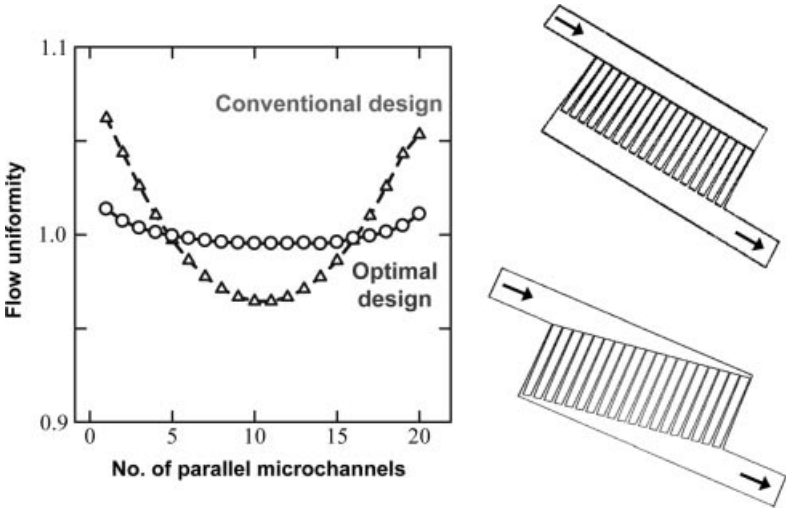

Figure 2.12 Fluid design results with normalized flows of wedge-shape inlet and outlet manifolds [24, 26]. The channel cross section is optimized for gas-phase chemical reaction and varies along the channel length. Interested readers are referred to the references.

2.7 Headers and Manifold for Plate Stacks

The appropriate flow manifold depends on the number of channels and the shape of the entire device. Microstructured devices for high flow rates often consist of a stack of microstructured plates. Experimental experience and proper integration of microstructured elements in a conventional apparatus are essential in order to design and fabricate this plate stack. The adjacent inlet and outlet chambers are designed according to fabrication issues, leading to large dead volumes, which spoil the narrow residence time distribution and allow backflow. The flow distribution and correct integration must be considered and is the most critical point for successful implementation. Depending on the size of the entire device, various fluidic manifolds or flow headers can be applied. The flow distribution on 8, 16, 32 and so on parallel channels can be managed with a fluidic manifold similar to the channel network for micro heat exchangers; see Section 2.4. Wada *et al.* [27] proposed a fluidic manifold for 16 microchannels with a width of 300 µm for a two-phase flow microreactor similar to the manifold in Figure 2.5a. The equal distribution is obtained via high pressure loss in a narrow channel section at the entrance of the reactor channel.

A manifold system with hose connectors was proposed by Schenk *et al.* [28] for internal and external numbering-up. The hose distribution system, supplying a

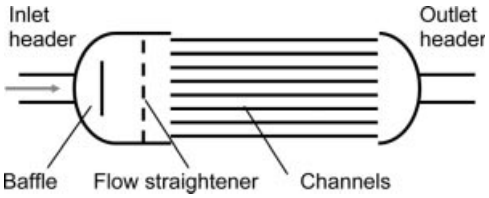

Figure 2.13 Schematic display of a tube bundle heat exchanger with manifold for flow distribution, consisting of baffle and flow straightener.

separation layer mixer, was designed with CFD simulation and lumped-element modeling and includes the header design for stacked microstructured plates.

For more than 20–30 channels on one plate, the dendritic fluidic manifold is difficult to design and high flow velocities in the channels lead to flow maldistribution due to vortex formation in the bends. Flow distribution as proposed in Section 2.6 are able to feed a multitude of channels uniformly. The flow distributor in Figure 2.13 is similar to flow headers in conventional tube bundle devices. At the entrance, the momentum of the inlet flow is directed to the side walls by a central plate, the baffle. Between the inlet plate and the microchannel entrance, a flow grid or straightener across the entire inlet section causes a small pressure loss and leads to uniform flow velocity over the entire header cross-section. With this arrangement, all channels of the microreactor face the same fluid velocity and are supplied with a uniform flow rate. This concept is known from wind tunnels to produce a uniform, homogeneous turbulent flow field in aerodynamic test sections. A more detailed description of microstructured equipment design is given in [10].

To yield a uniform fluid flow distribution in microreactors, a header configuration consisting of a cone diffuser connected to a thick-walled screen has been proposed by Rebrov *et al.* [29]. The thick-walled screen consists of an upstream section and a downstream section with elongated parallel channels, which are rotated 90° with respect to the upstream channels (Figure 2.14). The problem of flow distribution reduces to that of flow equalization in the channels of the thick-walled screen. CFD analysis of the fluid flow maldistribution indicates that eight parallel upstream channels with a width of 300–600 µm are required per 1 cm of length for flow equalization. The length to width ratio of these channels has to be larger than 15. The numerical results suggest that the ratio of the maximum flow velocity decreases to the mean flow velocity from 2 to less than 1% for a range of *Re* numbers from 0.5 to 10 in gas flow.

The minimum length between two neighboring downstream channels is $a = 400$ µm and the distance in cross-sectional view between a top wall of the first downstream channel and a side wall of the upstream channels is $b = 260$ µm. The width of the upstream channels c, the height of the downstream channels d and the distance between the neighboring upstream channels h are each 400 µm. The diameter of the channels in the microreactor (R) is usually equal to or slightly smaller than the distance d, so the distance in the vertical direction between the channels in

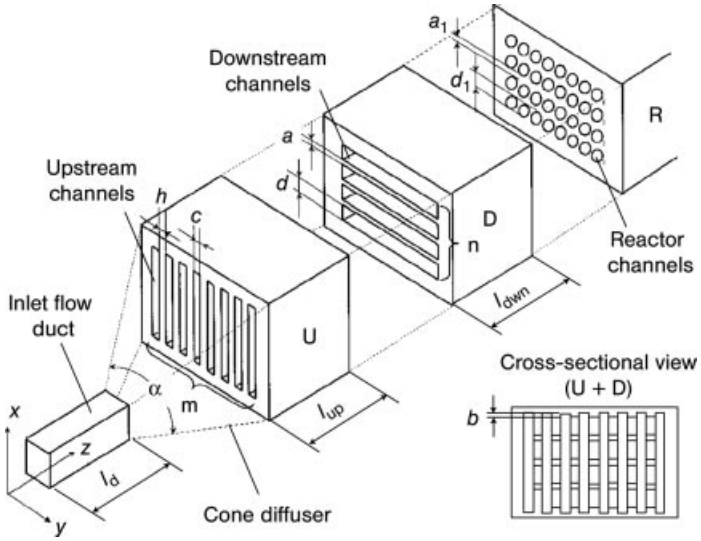

Figure 2.14 Flow distributor arrangement for catalytic microreactor according to Rebrov *et al*. [29]. The header consists of a cone diffuser and a thick-walled screen positioned in front of the microreactor.

the microreactor (a_1) is equal to or slightly greater than distance a. The diffuser expansion angle is not important for equalizing the fluid flow. An expansion angle close to 180° (sudden expansion) is also possible to minimize the dead volume of the header; however, the influence of backflow and dead zone on the residence time distribution has to be considered.

A CFD study indicated that at least eight upstream channels with a width of 300 µm are required per 1 cm of width of a thick-walled screen to provide flow non-uniformities less than 0.2%. The width of the upstream channels can be increased to 600 µm. However, this will double the flow non-uniformity and will shift the optimum distance between a top wall of the topmost downstream channel and a side wall of the upstream channel to higher values. The gain in equal flow supply to stacked plates is paid for by an enlarged pressure loss in the flow straightener. The authors did not report any data on the pressure loss. If the typical channel dimensions of the straightener are larger than the supplied stack, the pressure loss will be lower in the straightener. This additional pressure loss has to be taken into account for the design of flow manifolds.

2.8 Conclusion

To increase the flow rates in miniaturized devices, several strategies have been proposed, such as numbering-up, equaling-up and scaling-up. All concepts have

in common that they have to distribute the fluid on to several microstructured elements. Fluidic networks and inlet manifolds are proposed to distribute the fluid to parallel channels or fluidic elements on a single plate. Baffles and flow straighteners are suitable to distribute fluid flow uniformly to stacked plate devices. Lumped element modeling using a flow resistance network are employed to design larger networks and estimate manifold shape. CFD simulations with single elements are essential for single channel elements, especially for the transition flow regime for Reynolds numbers in the range 10–1000. The complete device is often too complex to simulate, and therefore biological principles (Murray's law) and a constructal approach according to Bejan assist the design process.

List of Symbols

A	channel cross-section [m^2]
b	channel width [m]
C_f	friction coefficient [−]
d_h	hydraulic diameter [m]
Dn	Dean number [−]
g	acceleration due to gravity [$m\,s^{-2}$]
h	channel height [m]
l	length [m]
l_p	length of wetted perimeter [m]
l_{in}	entrance length [m]
$\dot{m}$	mass flow rate [$kg\,s^{-1}$]
p	pressure [Pa]
R	bend radius [m]
Re	Reynolds number [−]
t	time [s]
w	velocity [$m\,s^{-1}$]
w_t	specific technical work [$W\,K^{-1}$]
x	Cartesian coordinate [m]
y	Cartesian coordinate [m]
z	level number of channel network

Greek Letters

Δp	pressure loss [Pa]
ζ	pressure loss coefficient [−]
η	dynamic viscosity [$kg\,m^{-1}\,s^{-1}$]
λ	channel friction factor [−]
ν	kinematic viscosity [$m^2\,s^1$]
ρ	density [$kg\,m^{-3}$]
φ_{12}	energy dissipation [$W\,kg^{-1}$]

References

1 N. Kockmann (ed.) *Micro Process Engineering*, Wiley-VCH Verlag GmbH, Weinheim, **2006**, pp. 99ff.

2 W. Albring, *Angewandte Strömungslehre*, Akademie-Verlag, Berlin, **1988**.

3 K.V. Sharp, R.J. Adrian, J.G. Santiago, J.I. Molho, Liquid flows in microchannels, in *MEMS Handbook*, ed. M. Gad-el-Hak, CRC Press, Boca Raton, FL, **2001**, Chapter 6.

4 H.D. Baehr, K. Stephan, *Wärme- und Stoffübertragung*, Springer, Berlin, **2004**.

5 K.H. Knoeck, *Fundamentals of Laminar Fluid Flow*, BJJS and Associates, Kerrimuir, Australia, **2000**.

6 F. Jiang, K. Drese, S. Hardt, M. Küpper, F. Schönfeld, Helical flows and chaotic mixing in curved micro channels *AIChE Journal*, **2004**, *50*, 2297–2305.

7 N. Kockmann, S. Dreher, P. Woias, Unsteady laminar flow regimes and mixing in T-shaped micromixers, Technical Paper, *ASME 5th International Conference on Nano-, Micro- and Minichannels, Puebla, Mexico*, **2007**, ICNMM2007-30041.

8 S. Dreher, N. Kockmann, P. Woias, Characterization of laminar transient flow regimes and mixing in T-shaped micromixers, *Heat Transfer Eng.*, **2008**, DOI 10.1080/01457630802293480.

9 R.K. Shah, A.L. London, *Laminar Forced Convection in Ducts*, Academic Press, New York, **1978**.

10 N. Kockmann, *Transport Phenomena in Micro Process Engineering*, Springer, Berlin, **2007**..

11 A. Bejan, *Shape and Structure, from Engineering to Nature*, Cambridge University Press, Cambridge, **2000**.

12 D.R. Emerson, K. Cieslicki, X. Gu, R.W. Barber, Biomimetic design of microfluidic manifolds based on a generalised Murray's law, *Lab Chip*, **2006**, *6*, 447–454.

13 Y. Chen, P. Cheng, An experimental investigation on the thermal efficiency of fractal tree-like microchannel nets, *Int. Commun. Heat Mass Transfer*, **2005**, *32*, 931–938.

14 A. Bejan, L.A.O. Rocha, S. Lorente, Thermodynamic optimization of geometry: T- and Y-shaped constructs of fluid streams, *Int. J. Therm. Sci.*, **2000**, *39*, 949–960.

15 A. Bejan, S. Lorente, The constructal law and the thermodynamics of flow systems with configuration, *Int. J. Heat Mass Transfer*, **2004**, *47*, 3203–3214.

16 T. Bello-Ochende, L. Liebenberg, J.P. Meyer, Constructal cooling channels for micro-channel heat sinks, *Int. J. Heat Mass Transfer*, **2007**, *50*, 4141–4150.

17 T.F. Sherman, On connecting large vessels to small. The meaning of Murray's law, *J. Gen. Physiol.*, **1981**, *78*, 431–453.

18 W. Konrad, A. Roth-Nebelsick, The significance of pit shape for hydraulic isolation of embolized conduits of vascular plants during novel refilling, *J. Biol. Phys.*, **2005**, *31*, 57–71.

19 A. Roth-Nebelsick, D. Uhl, V. Mosbrugger, H. Kerp, Evolution and function of leaf venation architecture: a review, *Ann. Bot.*, **2001**, *87*, 553–566.

20 G.B. West, J.H. Brown, B.J. Enquist, A general model for the origin of allometric scaling laws in biology, *Science*, **1997**, *276*, 122–126.

21 L. Sack, C.M. Streeter, N.M. Holbrook, Hydraulic analysis of water flow through leaves of sugar maple and red oak, *Plant Physiol.*, **2004**, *134*, 1824–1833.

22 H.M. Schaedel *Fluidische Bauelemente und Netzwerke*, Vieweg, Braunschweig, **1979**.

23 N. Kockmann, T. Kiefer, M. Engler, P. Woias, Channel networks for optimal heat transfer and high throughput mixers, ESI International Conference on Heat Transfer and Fluid Flow in Microscale, Il Ciocco, Italy, **2005**.

24 O. Tonomura, Simulation and analytical modeling for microreactor design, in *Micro Process Engineering*, ed. N.

Kockmann, Wiley-VCH Verlag GmbH, Weinheim, **2006**, Chapter 8.

25 P. Pfeifer, A. Wenka, K. Schubert, M.A. Liauw, G. Emig, Characterization of flow distribution in microchannel reactors, *AIChE J.*, **2004**, *50*, 418–425.

26 J.M. Commenge, L. Falk, J.P. Corriou, M. Matlosz, Optimal design for flow uniformity in microchannel reactors, *AIChE J.*, **2002**, *48*, 345–358.

27 Y. Wada, M.A. Schmidt, K.F. Jensen, Flow distribution and ozonolysis in gas–liquid multichannel microreactors, *Ind. Eng. Chem. Res.*, **2006**, *45*, 8036–8042.

28 R. Schenk, V. Hessel, C. Hofmann, J. Kiss, H. Löwe, F. Schönfeld, A. Ziogas, Numbering up von Mikroreaktoren: ein neues Flüssigkeitsverteilsystem, *Chem. Ing. Tech.*, **2004**, *76*, 584–597.

29 E.V. Rebrov, I.Z. Ismagilov, R.P. Ekatpure, M.H.J.M. de Croon, J.C. Schouten, Header design for flow equalization in microstructured reactors, *AIChE J.*, **2007**, *53*, 28–38.